Article

On-surface synthesis of aromatic cyclo[10] carbon and cyclo[14]carbon

Luye Sun[1,2], Wei Zheng[1,2], Wenze Gao[1], Faming Kang[1], Mali Zhao[1] & Wei Xu[1✉]

All-carbon materials based on sp^2-hybridized atoms, such as fullerenes[1], carbon nanotubes[2] and graphene[3], have been much explored due to their remarkable physicochemical properties and potential for applications. Another unusual all-carbon allotrope family are the cyclo[n]carbons (C_n) consisting of two-coordinated sp-hybridized atoms. They have been studied in the gas phase since the twentieth century[4–6], but their high reactivity has meant that condensed-phase synthesis and real-space characterization have been challenging, leaving their exact molecular structure open to debate[7–11]. Only in 2019 was an isolated C_{18} generated on a surface and its polyynic structure revealed by bond-resolved atomic force microscopy[12,13], followed by a recent report[14] on C_{16}. The C_{18} work trigged theoretical studies clarifying the structure of cyclo[n]carbons up to C_{100} (refs. 15–20), although the synthesis and characterization of smaller C_n allotropes remains difficult. Here we modify the earlier on-surface synthesis approach to produce cyclo[10]carbon (C_{10}) and cyclo[14]carbon (C_{14}) via tip-induced dehalogenation and retro-Bergman ring opening of fully chlorinated naphthalene ($C_{10}Cl_8$) and anthracene ($C_{14}Cl_{10}$) molecules, respectively. We use atomic force microscopy imaging and theoretical calculations to show that, in contrast to C_{18} and C_{16}, C_{10} and C_{14} have a cumulenic and cumulene-like structure, respectively. Our results demonstrate an alternative strategy to generate cyclocarbons on the surface, providing an avenue for characterizing annular carbon allotropes for structure and stability.

Early theory[21–24] predicted C_{10} to be the watershed between cyclic (for $n \geq 10$) and linear (for $n < 10$) C_n and the largest cumulenic aromatic cyclocarbon, whereas C_{14} is understood to be the point at which the cumulenic structure seen with C_{10} transitions, via Peierls distortion, to the polyynic structure seen with C_{18} (refs. 10,16,17). Investigating the structure of C_{10} and C_{14} is thus of particular interest.

Advanced scanning tunnelling microscopy (STM) and atomic force microscopy (AFM), especially when carried out with a CO-terminated tip, enable both bond-resolved characterization of molecular structures[25,26] and triggering of chemical reactions by manipulating individual atoms[27,28]. Importantly, in high-resolution AFM images of single molecules, polyynic moieties can be unambiguously distinguished from cumulenic moieties (that is, characteristic bright features of triple bonds and uniform line features of consecutive double bonds, respectively)[28,29].

The essential first step is the precise synthesis of C_{10} and C_{14} in the condensed phase, for which we follow earlier on-surface synthesis approaches in which molecules are stabilized on the surface, which is kept at extremely low temperatures. Inspired by the Bergman reaction[30] and previous methods generating carbon cluster ions[31,32], we used the reaction schemes shown in Fig. 1. As illustrated in Fig. 1a, Bergman and retro-Bergman reactions in solution involve a cyclization and a ring-opening reaction; the retro-Bergman ring-opening reaction has also been shown to be feasible on a surface (Fig. 1b)[33,34]. We used a fully

halogenated naphthalene (octachloronaphthalene, $C_{10}Cl_8$)[31] and anthracene (decachloroanthracene, $C_{14}Cl_{10}$) as molecular precursors, with the aim of generating C_{10} and C_{14} on the surface through tip-induced dehalogenation and retro-Bergman reactions (Fig. 1c,d).

The cyclo[10]carbon product can, in principle, adopt one of the four possible structures shown in Fig. 2. The two polyynic structures with D_{5h} and C_{5h} symmetries exhibit non-zero bond length alternations (BLA ≠ 0) (Fig. 2a,b), whereas the two cumulenic structures with D_{10h} and D_{5h} symmetries have zero bond length alternations (BLA = 0) (Fig. 2c,d). In contrast to the polyynic structure of C_{18} (refs. 10,16,17), calculations at different levels of theory (for example, density functional theory (DFT)[11,16,17] and coupled cluster methods[10,24]) have predicted a ground state for C_{10} with the D_{5h} cumulene geometry shown in Fig. 2d, and with BLA = 0 and bond angle alternation (BAA) ≠ 0 (see also detailed calculations in Extended Data Figs. 1 and 2).

For the experiments, all molecules were placed on a bilayer NaCl/Au(111) surface at 4.7 K. $C_{10}Cl_8$ was first introduced on the cold sample held at approximately 6 K and then imaged with STM (Extended Data Fig. 3a,b), revealing that single $C_{10}Cl_8$ molecules display an oval shape without internal features. In AFM images (Fig. 3a, (ii) and (iii)), the Cl atoms in $C_{10}Cl_8$ exhibit different contrasts in brightness. The brightness differences imply differences in adsorption heights caused by steric hindrance of Cl atoms in the highly strained molecule[34], confirmed by AFM simulations (Fig. 3a, (iv) and (v)). In the Laplace-filtered AFM image

[1]Interdisciplinary Materials Research Center, School of Materials Science and Engineering, Tongji University, Shanghai, People's Republic of China. [2]These authors contributed equally: Luye Sun, Wei Zheng. ✉e-mail: xuwei@tongji.edu.cn
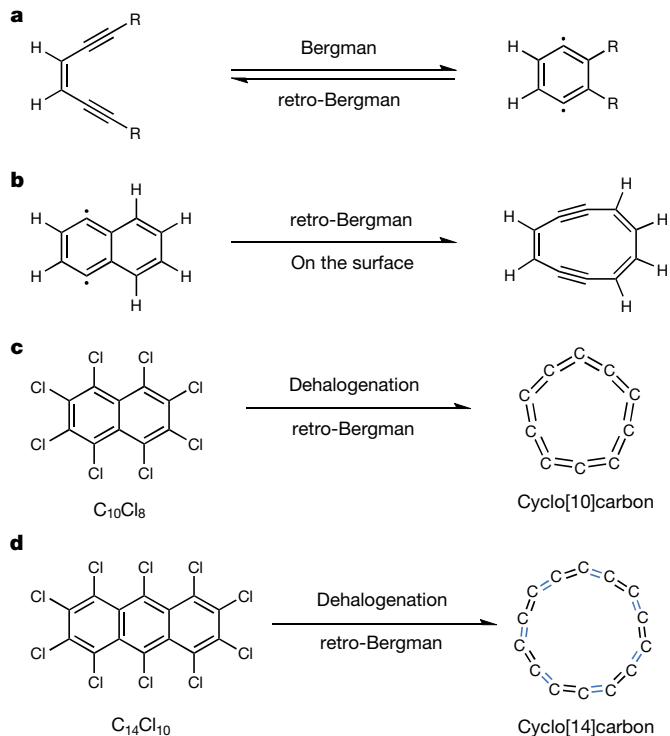
Fig. 1 | Reaction schemes for the formation of cyclo[10]carbon and cyclo[14] carbon. a, Bergman cyclization and its reverse process (retro-Bergman) involving a cyclization and a ring-opening reaction. **b**, The on-surface retro-Bergman ring-opening reaction. **c**,**d**, Reaction schemes for the formation of cyclo[10]carbon (**c**) and cyclo[14]carbon (**d**) by dehalogenation and retro-Bergman reactions. The double bonds indicated by blue and black in **d** represent two different bond lengths within cyclo[14]carbon.

(Fig. 3a, (vi)), more prominent features associated with the positions of Cl atoms in $C_{10}Cl_8$ are seen.

To remove Cl atoms from the molecule, the tip was initially positioned on a single molecule, and retracted by about 4 Å from the STM set point (typically $I = 1$ pA, $V = 0.3$ V) and the sample bias then gradually increased from 0.3 V to 4 V. This process typically resulted in the loss of two or three Cl atoms, yielding $C_{10}Cl_6$ or $C_{10}Cl_5$ intermediates that were structurally characterized by AFM imaging and the structures were confirmed by AFM simulations (Fig. 3b,c, (ii)–(vi), and Extended Data Fig. 4a–c). Note that the retro-Bergman ring-opening reaction has not occurred yet in the $C_{10}Cl_5$ molecule, which has two of its α-Cl atoms removed from the left carbon ring. Further voltage sweeping resulted in successive further dehalogenation of the $C_{10}Cl_6$ and $C_{10}Cl_5$ intermediates and usually yielded $C_{10}Cl_1$ or $C_{10}Cl_2$ intermediates consisting of a single carbon ring (Fig. 3d, (ii)–(vi), and Extended Data Fig. 4d–f), and thus suggesting occurrence of the retro-Bergman ring-opening reaction. The tip-induced dehalogenation could be related to anionic charge states of molecules or an applied electric field[34,35]. In addition, inelastic electron tunnelling may also help to trigger dehalogenative reactions[12].

Further voltage sweeping induced complete dehalogenation of the intermediates and generated the final product, as shown in the STM image (Extended Data Fig. 3c) and AFM images (Fig. 3e, (ii)–(iii)). The images clearly show that the final product contains a carbon ring, which could be unambiguously assigned to a single C_{10}. In addition, the C_{10} molecule represents a uniform feature in AFM images resembling the cumulenic structures reported before[29] and differing from the characteristic bright features seen with polyynic C_{18} and C_{16} (refs. 12–14). This naturally indicates a cumulenic structure for C_{10}, in excellent agreement with theoretical calculations (BLA = 0) (Extended Data Fig. 1)[10,11,16,17,24].

Further analysis of the AFM images (Fig. 3e (ii),(iii),(vi)) reveals that the C_{10} structure deviates from the structure of a perfect circle. Optimizing the C_{10} structure placed on different NaCl surface sites (Extended Data Fig. 5a–d) does not noticeably change the five-fold symmetry, indicating that this pentagon-like shape appearing in the AFM images (even if only faintly resolved) is probably related to the theoretically predicted intrinsic D_{5h} symmetry of C_{10} (shown in Fig. 2d). Note that AFM images acquired at a smaller oscillation amplitude (50 pm) exhibited similar features both in 'AFM far' and 'AFM close' images (Extended Data Fig. 6). Also note that C_{10} shows remarkable stability under our manipulation conditions ($V \le 4$ V), retaining its cyclic structure.

Calculations based on modern theory[10,16,17] for cyclo[14]carbon indicate that the ground state is a Peierls-transition intermediate with a structure between that of the cumulenic C_{10} and the polyynic C_{18}. Figure 4a shows the six possible C_{14} structures considered, with our calculations indicating a BAA of 25.3° (Extended Data Fig. 7) for the ground state, and a small BLA of 0.05 Å, which lies between the values for C_{10} (BLA = 0; Extended Data Fig. 1) and C_{18} (BLA = 0.12 Å; Extended Data Fig. 8)[17]. Such a Peierls-transition structure corresponds to a C_{7h} intermediate (Fig. 4a, (iv)), with the optimized structures for C_{14} adsorbed at Cl-top and Na-top sites on the NaCl surface shown in Extended Data Fig. 5e–h.

Analogous to the on-surface synthesis strategy used with C_{10}, we used the molecular precursor $C_{14}Cl_{10}$ for generating C_{14} (Fig. 1d). $C_{14}Cl_{10}$ precursor molecules were introduced onto a bilayer NaCl surface held at approximately 6 K. Due to steric hindrance experienced by the Cl atoms in the highly strained molecule, $C_{14}Cl_{10}$ exhibits a non-planar configuration in both STM and AFM images (Extended Data Fig. 9a–c). As with C_{10}, atom manipulation induces complete dehalogenation of the precursor and is accompanied by two-step retro-Bergman ring opening to give the C_{14} product on the surface with a yield of approximately 24% (see STM and AFM images and simulations in Extended Data Fig. 9e and Fig. 4b–d). AFM imaging at different heights (Fig. 4b, (i)–(iii)) shows that the final product has a carbon ring that is unambiguously assigned to a single C_{14}. In all AFM-derived images, C_{14} exhibits a cumulenic feature resembling that of C_{10}, despite a BLA of 0.05 Å calculated for the former. We therefore assign a cumulene-like structure for C_{14}, which is also obviously different from the polyynic C_{18} and C_{16} with characteristic bright features. We note that a BLA of only 0.05 Å cannot be distinguished experimentally by AFM imaging, so more detailed structural characterization of C_{14} was performed by AFM image simulations, as shown in Fig. 4e (more details are shown in Extended Data Fig. 10). We simulated AFM images of C_{14} with varying BLAs, ranging from cumulenic to intermediate and polyynic structures (that is, BLA = 0, 0.03 Å, 0.05 Å, 0.07 Å, 0.09 Å, 0.11 Å, 0.13 Å, 0.15 Å), to explore the limits of AFM imaging for differentiating between structures with different BLAs. The simulations suggest that, in the case of 0 < BLA < 0.09 Å, which covers the Peierls-transition region, structures can be assigned as cumulene-like, although they are difficult to differentiate. When BLA ≥ 0.09 Å, structures can be identified as polyynic, and larger BLAs give rise to more pronounced bright features over the triple bonds.

Cyclo[14]carbon formation and the accompanying skeletal rearrangements were further probed by investigating the intermediates
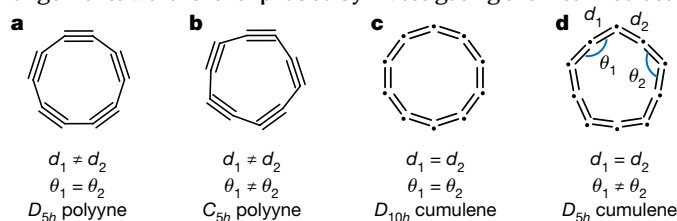

Fig. 2 | Four possible structures of cyclo[10]carbon. a–d, The polyynic forms with D_{5h} (**a**) and C_{5h} (**b**) symmetries, and the cumulenic forms with D_{10h} (**c**) and D_{5h} (**d**) symmetries are shown. The bond length alternation is defined as BLA = $d_1 - d_2$ and the bond angle alternation is defined as BAA = $\theta_1 - \theta_2$.
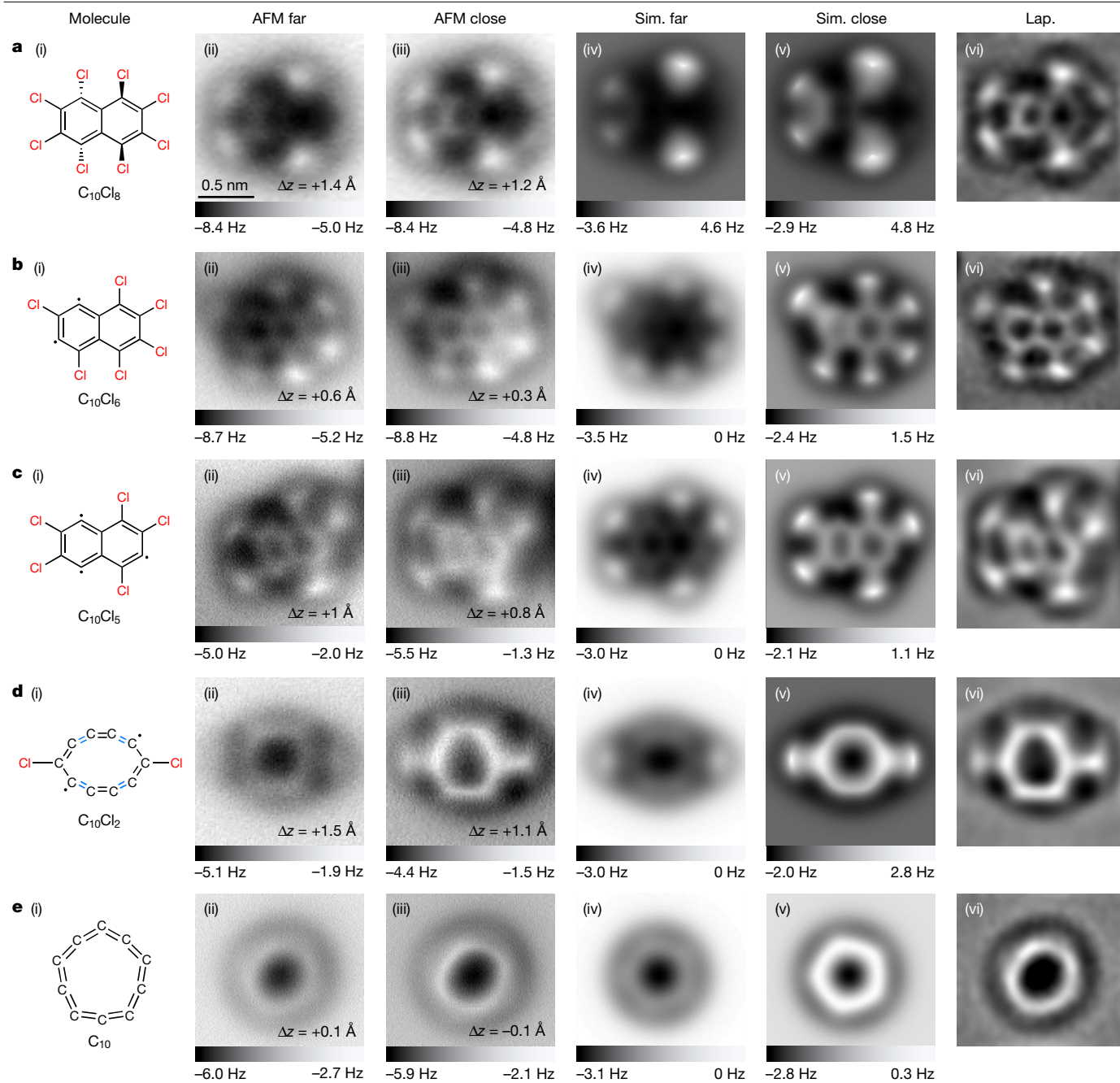
Fig. 3 | On-surface generated precursor, intermediates and product (C$_{10}$).
a, Precursor images. **b**–**d**, The most frequently observed reaction intermediates: C$_{10}$Cl$_6$ (**b**); C$_{10}$Cl$_5$ (**c**); C$_{10}$Cl$_2$ (**d**). **e**, Cyclo[10]carbon. Images shown are: (i) molecular structures; (ii) and (iii) AFM images; (iv) and (v) AFM simulations (sim.); (vi) Laplace-filtered (Lap.) AFM images. The double bonds indicated by blue and black in **d** (i) represent two different bond lengths within C$_{10}$Cl$_2$. AFM images were recorded with a CO-terminated tip at different tip offsets, Δz, with respect to STM set points (**a** (ii)–(iii), **b** (ii)–(iii): $I = 1$ pA, $V = 0.3$ V; **c** (ii)–(iii), **d** (ii)–(iii): $I = 2$ pA, $V = 0.3$ V; **e** (ii)–(iii): $I = 0.5$ pA, $V = 0.3$ V) above the NaCl surface. AFM simulations are based on gas-phase DFT-calculated geometries. The scale bar in **a** (ii) applies to all experimental, simulated and Laplace-filtered AFM images.

involved, using AFM imaging and simulations (Fig. 4f–h). Dehalogenation of the intermediate C$_{14}$Cl$_6$ (Fig. 4f) results in the formation of C$_{14}$Cl$_4$, which consists of a ten-membered ring with characteristic bright features above the triple bonds resolved (Fig. 4g); this suggests that the first-step retro-Bergman reaction has occurred. Further dehalogenation leads to the formation of C$_{14}$Cl$_1$, imaged as a larger carbon ring that lacks characteristic bright features and with one Cl atom attached; this suggests that the second-step retro-Bergman reaction has occurred (Fig. 4h). Compared to the ten-membered ring of the preceding C$_{14}$Cl$_4$ intermediate, the experimental observations and calculations both indicate that the BLA decreases for most C–C bonds within the C$_{14}$Cl$_1$

ring (Extended Data Figs. 11 and 12 (for other intermediates and side reaction products)).

To conclude, our successful generation of the aromatic cyclo[10] carbon and cyclo[14]carbon by atom manipulation on the bilayer NaCl/ Au(111) surface at 4.7 K has enabled us to confirm a cumulenic structure for C$_{10}$ by bond-resolved AFM imaging, as predicted by theory. More interestingly, the experimental AFM images of the Peierls-transition intermediate C$_{14}$ also show cumulenic characteristics. Although the AFM imaging resolution is not sufficient to detect the small bond length alternation of 0.05 Å calculated for this molecule, it does identify C$_{14}$ as an intermediate structure between the cumulenic C$_{10}$ and the polyynic
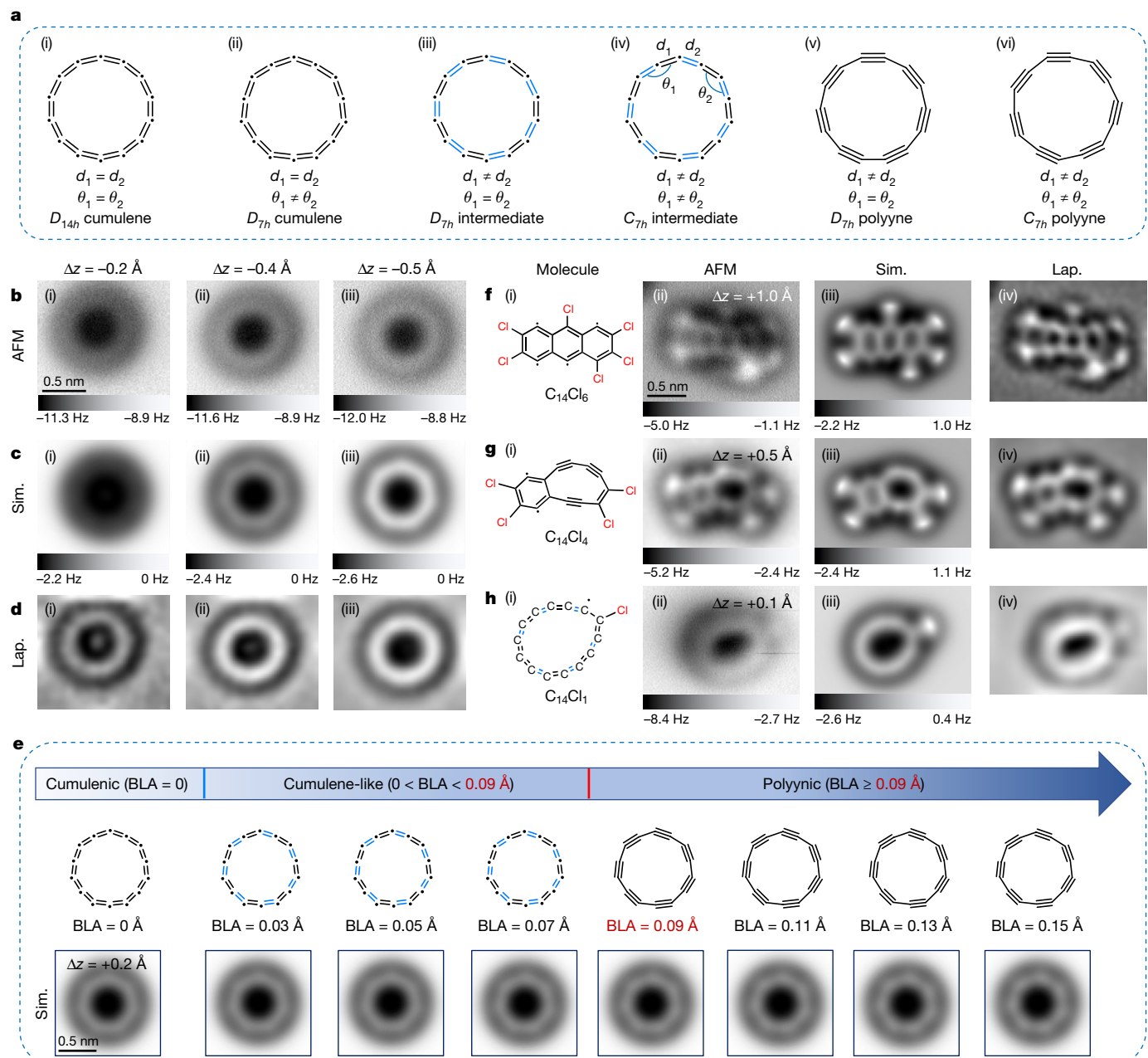
Fig. 4 | On-surface generated intermediates, product (C₁₄) and AFM simulations of C₁₄ with varying BLAs. a, Six possible structures of cyclo[14] carbon. The cumulenic forms with D_{14h} (i) and D_{7h} (ii) symmetries, the intermediate structures with D_{7h} (iii) and C_{7h} (iv) symmetries, and the polyyinic forms with D_{7h} (v) and C_{7h} (vi) symmetries are shown. The bond length alternation is defined as BLA = $d_1 - d_2$ and the bond angle alternation is defined as BAA = $\theta_1 - \theta_2$. **b**–**d**, AFM images (**b** (i)–(iii)), AFM simulations (**c** (i)–(iii)) and Laplace-filtered AFM images (**d** (i)–(iii)) of cyclo[14]carbon at different tip heights. **e**, AFM simulations of C₁₄ with varying BLAs. **f**–**h**, Intermediates C₁₄Cl₆ (**f** (i)–(iv)), C₁₄Cl₄ (**g** (i)–(iv)) and C₁₄Cl₁ (**h** (i)–(iv)). The double bonds indicated by blue and black in **a** (iii),(iv), **h** (i) and **e** represent two different bond lengths within the structures, respectively. AFM images were recorded with a CO-terminated tip at different tip offsets, Δz, with respect to STM set point (**b** (i)–(iii), **f** (ii), **g** (ii) and **h** (ii): I = 1 pA, V = 0.3 V) above the NaCl surface. AFM simulations are based on gas-phase DFT-calculated geometries. The scale bar in **b** (i) applies to all experimental, simulated AFM and Laplace-filtered images of cyclo[14]carbon. The scale bar in **f** (ii) applies to all experimental, simulated AFM and Laplace-filtered images of intermediates. The scale bar in **e** applies to all simulated AFM images with varying BLAs.

C₁₈. We anticipate that the complement of our and previous on-surface synthesis strategies will enable the generation of other cyclo[*n*]carbons that might exhibit interesting properties.

Online content

Any methods, additional references, Nature Portfolio reporting summaries, source data, extended data, supplementary information,

1. Kroto, H. W., Heath, J. R., O'Brien, S. C., Curl, R. F. & Smalley, R. E. C₆₀: buckminsterfullerene. *Nature* **318**, 162–163 (1985).
2. Iijima, S. & Ichihashi, T. Single-shell carbon nanotubes of 1-nm diameter. *Nature* **363**, 603–605 (1993).

Article

3.   Novoselov, K. S. et al. Electric field effect in atomically thin carbon films. *Science* **306**, 666–669 (2004).
4.   Parent, D. C. & McElvany, S. W. Investigations of small carbon cluster-ion structures by reactions with hydrogen cyanide. *J. Am. Chem. Soc.* **111**, 2393–2401 (1989).
5.   Van Orden, A. & Saykally, R. J. Small carbon clusters: spectroscopy, structure, and energetics. *Chem. Rev.* **98**, 2313–2357 (1998).
6.   Grutter, M. et al. Electronic absorption spectra of linear C_6, C_8 and cyclic C_{10}, C_{12} in neon matrices. *J. Chem. Phys.* **111**, 7397–7401 (1999).
7.   Pitzer, K. S. & Clementi, E. Large molecules in carbon vapor. *J. Am. Chem. Soc.* **81**, 4477–4485 (1959).
8.   Parasuk, V., Almlof, J. & Feyereisen, M. W. The [18] all-carbon molecule: cumulene or polyacetylene? *J. Am. Chem. Soc.* **113**, 1049–1050 (1991).
9.   Torelli, T. & Mitas, L. Electron correlation in C_{4N+2} carbon rings: aromatic versus dimerized structures. *Phys. Rev. Lett.* **85**, 1702–1705 (2000).
10. Arulmozhiraja, S. & Ohno, T. CCSD calculations on C_{14}, C_{18}, and C_{22} carbon clusters. *J. Chem. Phys.* **128**, 114301 (2008).
11. Remya, K. & Suresh, C. H. Carbon rings: a DFT study on geometry, aromaticity, intermolecular carbon–carbon interactions and stability. *RSC Adv.* **6**, 44261–44271 (2016).
12. Kaiser, K. et al. An *sp*-hybridized molecular carbon allotrope, cyclo[18]carbon. *Science* **365**, 1299–1301 (2019).
13. Scriven, L. M. et al. Synthesis of cyclo[18]carbon via debromination of $C_{18}Br_6$. *J. Am. Chem. Soc.* **142**, 12921–12924 (2020).
14. Gao, Y. et al. On-surface synthesis of a doubly anti-aromatic carbon allotrope. *Nature* https://doi.org/10.1038/s41586-023-06566-8 (2023).
15. Baryshnikov, G. V., Valiev, R. R., Kuklin, A. V., Sundholm, D. & Agren, H. Cyclo[18]carbon: insight into electronic structure, aromaticity, and surface coupling. *J. Phys. Chem. Lett.* **10**, 6701–6705 (2019).
16. Baryshnikov, G. V. et al. Aromaticity of even-number cyclo[*n*]carbons (*n*=6–100). *J. Phys. Chem. A* **124**, 10849–10855 (2020).
17. Charistos, N. D. & Muñoz-Castro, A. Induced magnetic field in *sp*-hybridized carbon rings: analysis of double aromaticity and antiaromaticity in cyclo[2*N*]carbon allotropes. *Phys. Chem. Chem. Phys.* **22**, 9240–9249 (2020).
18. Baryshnikov, G. V. et al. Odd-number cyclo[*n*]carbons sustaining alternating aromaticity. *J. Phys. Chem. A* **126**, 2445–2452 (2022).
19. Brémond, E., Pérez-Jiménez, A. J., Adamo, C. & Sancho-García, J. C. Stability of the polyynic form of C_{18}, C_{22}, C_{26}, and C_{30} nanorings: a challenge tackled by range-separated double-hybrid density functionals. *Phys. Chem. Chem. Phys.* **24**, 4515–4525 (2022).
20. Li, M. et al. Potential molecular semiconductor devices: cyclo-C_n (*n*=10 and 14) with higher stabilities and aromaticities than acknowledged cyclo-C_{18}. *Phys. Chem. Chem. Phys.* **22**, 4823–4831 (2020).
21. Hoffmann, R. Extended Hückel theory——V: cumulenes, polyenes, polyacetylenes and C_n. *Tetrahedron* **22**, 521–538 (1966).
22. Liang, C. & Schaefer, H. F. III Carbon clusters: the structure of C_{10} studied with configuration interaction methods. *J. Chem. Phys.* **93**, 8844–8849 (1990).
23. Hutter, J., Lüthi, H. P. & Diederich, F. Structures and vibrational frequencies of the carbon molecules C_2–C_{18} calculated by density functional theory. *J. Am. Chem. Soc.* **116**, 750–756 (1994).
24. Watts, J. D. & Bartlett, R. J. The nature of monocyclic C_{10}. A theoretical investigation using coupled-cluster methods. *Chem. Phys. Lett.* **190**, 19–24 (1992).
25. Gross, L., Mohn, F., Moll, N., Liljeroth, P. & Meyer, G. The chemical structure of a molecule resolved by atomic force microscopy. *Science* **325**, 1110–1114 (2009).
26. Gross, L. et al. Bond-order discrimination by atomic force microscopy. *Science* **337**, 1326–1329 (2012).
27. Pavliček, N. et al. On-surface generation and imaging of arynes by atomic force microscopy. *Nat. Chem.* **7**, 623–628 (2015).
28. Pavliček, N. et al. Polyyne formation via skeletal rearrangement induced by atomic manipulation. *Nat. Chem.* **10**, 853–858 (2018).
29. Sun, Q. et al. On-surface formation of cumulene by dehalogenative homocoupling of alkenyl gem-dibromides. *Angew. Chem. Int. Ed. Engl.* **56**, 12165–12169 (2017).
30. Jones, R. R. & Bergman, R. G. *p*-Benzyne. Generation as an intermediate in a thermal isomerization reaction and trapping evidence for the 1,4-benzenediyl structure. *J. Am. Chem. Soc.* **94**, 660–661 (1972).
31. Lifshitz, C., Peres, T., Kababia, S. & Agranat, I. C_{10}^+ and C_7^+ carbon cluster ions from overcrowded octachloropentafulvalene and octachloronaphthalene. *Int. J. Mass Spectrom. Ion Processes* **82**, 193–204 (1988).
32. Lifshitz, C., Peres, T. & Agranat, I. Properties of carbon cluster ions, C_n^+, formed by dissociative ionization. *Int. J. Mass Spectrom. Ion Processes* **93**, 149–163 (1989).
33. Schuler, B. et al. Reversible Bergman cyclization by atomic manipulation. *Nat. Chem.* **8**, 220–224 (2016).
34. Albrecht, F. et al. Selectivity in single-molecule reactions by tip-induced redox chemistry. *Science* **377**, 298–301 (2022).
35. Suresh, R. et al. Cyclo[18]carbon formation from $C_{18}Br_6$ and $C_{18}(CO)_6$ precursors. *J. Phys. Chem. Lett.* **13**, 10318–10325 (2022).

Methods

Experimental details for STM and AFM measurements

STM and AFM measurements were carried out in a commercial (Createc) low-temperature system operated at 4.7 K with base pressure better than 1×10^{-10} mbar. Single crystalline Au(111) surface was cleaned by several sputtering and annealing cycles. The NaCl films were obtained by thermally evaporating NaCl crystals onto a clean Au(111) surface at room temperature, resulting in islands of two and three monolayer thickness. Octachloronaphthalene ($C_{10}Cl_8$, purchased from Aladdin, greater than 99%) and decachloroanthracene ($C_{14}Cl_{10}$, synthesized using procedures in ref. 36) molecules were deposited on a cold NaCl/Au(111) surface by thermal sublimation from a molecular evaporator. CO molecules for tip modification[25] were dosed onto the cold sample via a leak valve. We used a qPlus sensor[37] with a resonance frequency $f_0 = 29.49$ kHz, quality factor $Q \approx 45,000$ and a spring constant $k \approx 1,800$ N m^{-1} operated in frequency-modulation mode[38]. The bias voltage V was applied to the sample with respect to the tip. AFM images were acquired in constant-height mode at $V = 0$ V and an oscillation amplitude of $A = 1$ Å (unless otherwise noted). The tip-height offsets, Δz, for constant-height AFM images are defined as the offset in tip-sample distance relative to the STM set point at the NaCl surface. The positive (negative) values of Δz correspond to the tip-sample distance increased (decreased) with respect to a STM set point.

DFT calculations and AFM simulations

DFT calculations were carried out in the gas phase using the Gaussian 16 program package[39]. The ωB97XD exchange-correlation functional[40] in conjunction with 6-311++G(d,p)[41] basis sets was used for all C_{10} and C_{14} related calculations in the gas phase[17]. The electrostatic potentials, localized orbital locator (LOL) and interaction region indicator (IRI) of molecules were calculated at the ωB97XD/6-311++G(d,p) level combined with Multiwfn v.3.8 code[42] and Visual Molecular Dynamics (VMD v.1.9)[43].

The AFM simulations were conducted using the PP-AFM code provided by Hapala et al.[44]. The detailed parameters are listed below. The lateral spring constant for the CO tip was 0.2 N m^{-1}, and a quadrupole-like charge distribution at the tip apex was used to simulate the CO tip with $q = -0.05e$ (e is the elementary charge and refers to $|e|$, and q is the magnitude of quadrupole charge at the tip apex). The amplitude was set as 1 Å (unless otherwise noted). The difference in probe height between 'sim. far' and 'sim. close' corresponded to the respective difference between 'AFM far' and 'AFM close'.

The Vienna ab initio simulation package[45,46] was used to perform DFT calculations on the NaCl surface. For describing the interaction between electrons and ions, the projector-augmented wave method[47,48] was used, and the Perdew–Burke–Ernzerhof generalized gradient approximation exchange-correlation functional was used[49]. The van der Waals corrections to the Perdew–Burke–Ernzerhof density functional were also included using the DFT-D3 method of Grimme[50]. The kinetic energy cutoff was set to 400 eV. We used a bilayer NaCl(001) slab separated by a vacuum thicker than 20 Å and the bottom layer of the NaCl was fixed. The atomic structures were relaxed until the atomic forces were less than 0.03 eV Å^{-1}.

Theoretical calculations were used to gain more insight into the electronic structures of C_{10}. As an sp-hybridized carbon allotrope, C_{10} generally possesses two perpendicular π-conjugated electron systems (in-plane and out-of-plane π molecular orbitals (π_{in} and π_{out} MOs)), thus we performed the LOL function to reveal the delocalization of π electrons in the cumulenic C_{10} ring on the basis of π MOs. As illustrated in the LOL-π_{in} and LOL-π_{out} isosurface maps (Extended Data Fig. 2a,c), the favourable global delocalization channels of the electrons in π_{in} and π_{out} MOs are clearly depicted. More importantly, the isosurfaces around all C–C bonds are volumetrically similar, indicating that the electrons over all C–C bonds are equally delocalized, which is significantly different

from the C_{18} with alternating bond lengths[20,51]. The colour-filled LOL-π map draws the same conclusion from a complementary perspective (Extended Data Fig. 2b,d). The IRI analysis was also performed to reveal the interactions within the C_{10}. As shown in the IRI isosurface (Extended Data Fig. 2e), both covalent bond and van der Waals interaction regions are nicely revealed by the blue and green isosurfaces, respectively, according to the standard colouring method (Extended Data Fig. 2g)[52]. Notably, the covalent interactions (blue isosurfaces) in all C–C bonds are homogeneous, indicating no bond length alternation, which is consistent with the IRI colour-filled map (Extended Data Fig. 2f) and LOL results. Thus, both the LOL and IRI analyses exhibited that all the C–C bonds in cyclo[10]carbon are identical, further indicating that the C_{10} ring is cumulenic, in accordance with the conclusion drawn by bond order analysis (Extended Data Fig. 1).

The standard colouring method and chemical explanation of sign(λ_2)ρ on the IRI isosurfaces are shown in Extended Data Fig. 2g. The IRI function is defined as follows:

$$\text{IRI}(\mathbf{r}) = \frac{|\nabla \rho(\mathbf{r})|}{[\rho(\mathbf{r})]^a} \tag{1}$$

where ρ is the electron density, $\mathbf{r}$ is the coordinate vector and a is an adjustable parameter, $a = 1.1$ is adopted for the standard definition of IRI[52]. The isosurfaces of IRI can exhibit various kinds of interaction regions by properly choosing isovalue. The sign(λ_2) denotes the sign of the second largest eigenvalue of Hessian of ρ, which has a certain ability to distinguish attractive and repulsive interactions[42,53]. The region showing relatively high ρ and thus large magnitude of sign(λ_2)ρ implies a relatively strong interaction, whereas the area with low ρ and thus small sign(λ_2)ρ does not participate in a noticeable interaction, or the interaction can be at most attributed to the very weak interatomic van der Waals interaction[52].

Data availability

All data supporting the findings of this study are available within the paper and its online Extended Data files.

36. Dobrowolski, M. A., Cyranski, M. K. & Wrobel, Z. Cyclic π-electron delocalization in non-planar linear acenes. *Phys. Chem. Chem. Phys.* **18**, 11813–11820 (2016).
37. Giessibl, F. J. High-speed force sensor for force microscopy and profilometry utilizing a quartz tuning fork. *Appl. Phys. Lett.* **73**, 3956–3958 (1998).
38. Albrecht, T. R., Grütter, P., Horne, D. & Rugar, D. Frequency modulation detection using high-Q cantilevers for enhanced force microscope sensitivity. *J. Appl. Phys.* **69**, 668–673 (1991).
39. Frisch, M. J. et al. *Gaussian 16 Rev. C.01* (Gaussian, 2016).
40. Chai, J. D. & Head-Gordon, M. Long-range corrected hybrid density functionals with damped atom–atom dispersion corrections. *Phys. Chem. Chem. Phys.* **10**, 6615–6620 (2008).
41. Hehre, W. J. Ab initio molecular orbital theory. *Acc. Chem. Res.* **9**, 399–406 (1976).
42. Lu, T. & Chen, F. Multiwfn: a multifunctional wavefunction analyzer. *J. Comput. Chem.* **33**, 580–592 (2012).
43. Humphrey, W., Dalke, A. & Schulten, K. VMD: visual molecular dynamics. *J. Mol. Graph.* **14**, 33–38 (1996).
44. Hapala, P. et al. Mechanism of high-resolution STM/AFM imaging with functionalized tips. *Phys. Rev. B* **90**, 085421 (2014).
45. Kresse, G. & Hafner, J. *Ab initio* molecular dynamics for open-shell transition metals. *Phys. Rev. B* **48**, 13115–13118 (1993).
46. Kresse, G. & Furthmüller, J. Efficient iterative schemes for *ab initio* total-energy calculations using a plane-wave basis set. *Phys. Rev. B* **54**, 11169–11186 (1996).
47. Blöchl, P. E. Projector augmented-wave method. *Phys. Rev. B* **50**, 17953–17979 (1994).
48. Kresse, G. & Joubert, D. From ultrasoft pseudopotentials to the projector augmented-wave method. *Phys. Rev. B* **59**, 1758–1775 (1999).
49. Perdew, J. P., Burke, K. & Ernzerhof, M. Generalized gradient approximation made simple. *Phys. Rev. Lett.* **77**, 3865–3868 (1996).
50. Grimme, S., Antony, J., Ehrlich, S. & Krieg, H. A consistent and accurate *ab initio* parametrization of density functional dispersion correction (DFT-D) for the 94 elements H–Pu. *J. Chem. Phys.* **132**, 154104 (2010).
51. Liu, Z., Lu, T. & Chen, Q. An *sp*-hybridized all-carboatomic ring, cyclo[18]carbon: bonding character, electron delocalization, and aromaticity. *Carbon* **165**, 468–475 (2020).
52. Lu, T. & Chen, Q. Interaction region indicator: a simple real space function clearly revealing both chemical bonds and weak interactions. *Chem. Methods* **1**, 231–239 (2021).
53. Johnson, E. R. et al. Revealing noncovalent interactions. *J. Am. Chem. Soc.* **132**, 6498–6506 (2010).

Article

Author contributions W.X. conceived the research. L.S., W.G. and F.K. performed the STM/AFM experiments and carried out the DFT calculations. W.Z. synthesized the $C_{14}Cl_{10}$ molecules. All authors contributed to writing the manuscript.

Competing interests The authors declare no competing interests.

Additional information
Correspondence and requests for materials should be addressed to Wei Xu.
Peer review information *Nature* thanks Glib Baryshnikov and the other, anonymous, reviewer(s) for their contribution to the peer review of this work.
**Reprints and permissions information** is available at http://www.nature.com/reprints.
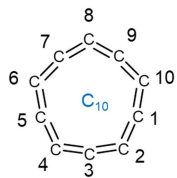
C-C-C	Bond angle (°)
1-2-3	123.264
2-3-4	164.744
3-4-5	123.262
4-5-6	164.738
5-6-7	123.230
6-7-8	164.796
7-8-9	123.203
8-9-10	164.790
9-10-1	123.235
10-1-2	164.735

C-C	Bond length(Å)	Bond order
1-2	1.2897	1.9426
2-3	1.2897	1.9426
3-4	1.2897	1.9425
4-5	1.2897	1.9427
5-6	1.2898	1.9429
6-7	1.2897	1.9412
7-8	1.2898	1.9410
8-9	1.2898	1.9421
9-10	1.2897	1.9408
10-1	1.2898	1.9432

Extended Data Fig. 1 | The bond lengths, Mayer bond orders and bond angles in a cyclo[10]carbon. Calculations were conducted at the ωB97XD/6-311 + + G (d,p) level. The bond lengths and bond order in C_{10} are all nearly the same, indicating the structure of consecutive carbon-carbon double bonds, i.e., cumulenic structure (BLA = 0).
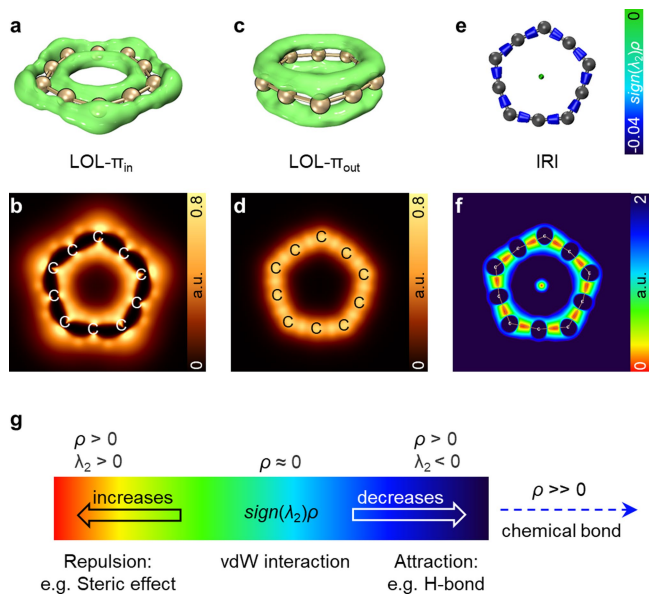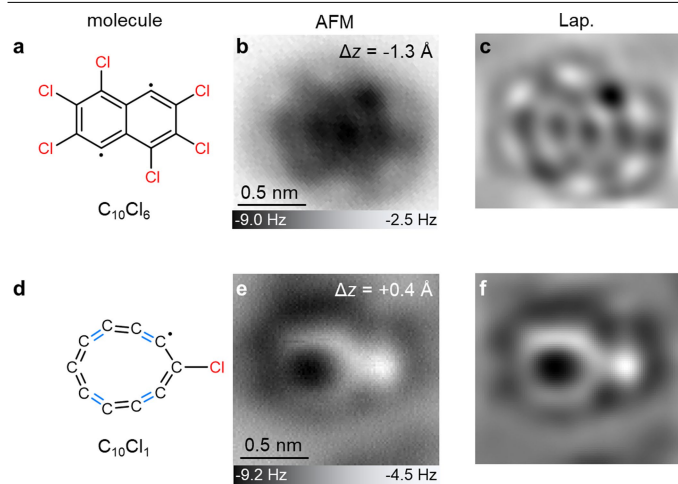
Extended Data Fig. 2 | Real-space function analysis of cyclo[10]carbon.
(**a** to **d**) Localized orbital locator calculated based on in-plane π MOs (LOL-π_{in})
and out-plane π MOs (LOL-π_{out}). (**a**) and (**c**) correspond to isosurface maps of
LOL-π = 0.4. (**b**) shows LOL-π_{in} in the ring plane, and (**d**) shows LOL-π_{out} above 1
Bohr of the ring plane. (**e**) Interaction region indicator (IRI) isosurface and
(**f**) color-filled map of C_{10} showing the homogeneous covalent interactions in
carbon-carbon bonds. (**g**) Standard coloring method and chemical explanation
of sign(λ_2)ρ on interaction region indicator (IRI) isosurfaces.
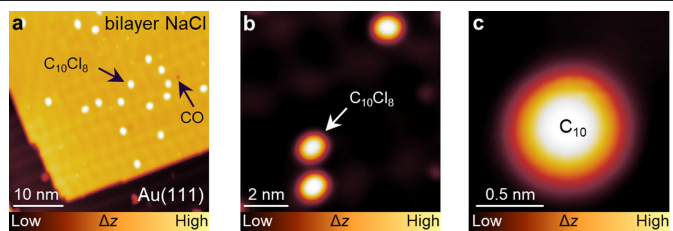
Extended Data Fig. 3 | STM images of the $C_{10}Cl_8$ precursor and the product cyclo[10]carbon. (**a**) $C_{10}Cl_8$ molecules separately adsorbed on bilayer NaCl/Au(111) surface. A single CO molecule appeared as a small depression. (**b**) Close-up STM image of single $C_{10}Cl_8$ molecules on NaCl. (**c**) Close-up STM image of C_{10}. Scanning condition: (**a**) $I = 1$ pA, $V = 0.3$ V. (**b**) $I = 2$ pA, $V = 0.3$ V. (**c**) $I = 0.5$ pA, $V = 0.3$ V.

molecule	AFM	Lap.

a

$C_{10}Cl_6$

b $\Delta z = -1.3$ Å

0.5 nm

-9.0 Hz   -2.5 Hz

c

d

$C_{10}Cl_1$

e $\Delta z = +0.4$ Å
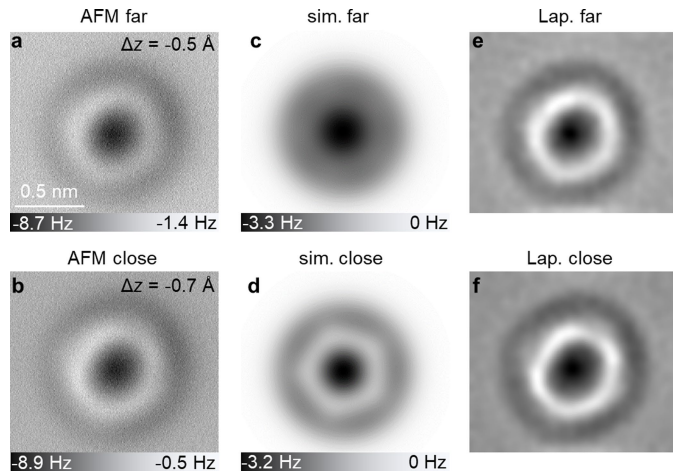

0.5 nm

-9.2 Hz   -4.5 Hz

f

Extended Data Fig. 4 | Other intermediates observed during manipulation.
(**a-c**) $C_{10}Cl_6$, (**d-f**) $C_{10}Cl_1$. The Laplace-filtered AFM images are also shown.
Reference set point of Δz: $I = 0.5$ pA, $V = 0.3$ V for (**b**), $I = 1$ pA, $V = 0.3$ V for (**e**).
The double bonds indicated by blue and black in (**d**) represent two different
bond lengths within the structure, respectively.

Cl-top site	Na-top site	Cl-top site	Na-top site
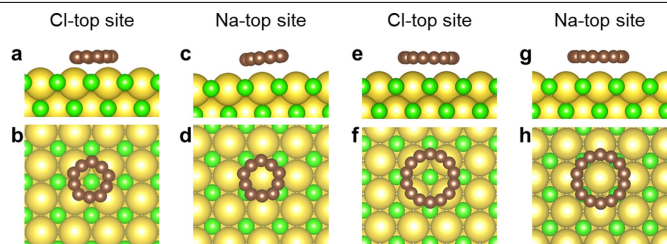
Extended Data Fig. 5 | DFT relaxed C_{10} and C_{14} structures on NaCl surface.
(**a**, **b**) C_{10} on Cl-top site. (**c**, **d**) C_{10} on Na-top site. (**e**, **f**) C_{14} on Cl-top site. (**g**, **h**) C_{14} on Na-top site.

AFM far

a Δz = -0.5 Å

0.5 nm

-8.7 Hz   -1.4 Hz

sim. far

c

-3.3 Hz   0 Hz

Lap. far

e

AFM close

b Δz = -0.7 Å

-8.9 Hz   -0.5 Hz

sim. close

d

-3.2 Hz   0 Hz

Lap. close

f

Extended Data Fig. 6 | AFM images of C_{10} acquired at the oscillation amplitude A = 50 pm. We tested the effect of different amplitude on the AFM imaging of C_{10}. The AFM image (**a**, **b**) and AFM simulations (**c**, **d**) were carried out at the oscillation amplitude A = 50 pm. The Laplace-filtered AFM images of (**a**) and (**b**) are also shown in (**e**) and (**f**). Reference set point of Δz: I = 0.5 pA, V = 0.3 V. The scale bar in (**a**) applies to all experimental, simulated and Laplace-filtered AFM images.
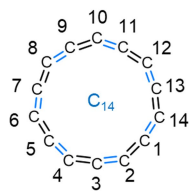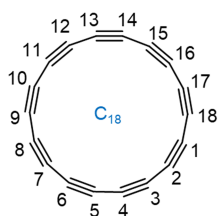
C-C	Bond length(Å)	Bond order
1-2	1.3073	1.7443
2-3	1.2560	2.0643
3-4	1.3074	1.7444
4-5	1.2561	2.0640
5-6	1.3073	1.7440
6-7	1.2561	2.0644
7-8	1.3072	1.7446
8-9	1.2562	2.0644
9-10	1.3072	1.7444
10-11	1.2561	2.0648
11-12	1.3073	1.7448
12-13	1.2560	2.0641
13-14	1.3075	1.7443
14-1	1.2561	2.0644

C-C-C	Bond angle (°)
1-2-3	141.645
2-3-4	166.941
3-4-5	141.621
4-5-6	166.958
5-6-7	141.623
6-7-8	166.931
7-8-9	141.632
8-9-10	166.938
9-10-11	141.662
10-11-12	166.910
11-12-13	141.644
12-13-14	166.940
13-14-1	141.617
14-1-2	166.939

Extended Data Fig. 7 | The bond lengths, Mayer bond orders and bond angles in a cyclo[14]carbon. Calculations were conducted at the ωB97XD/6-311 + + G(d,p) level, revealing a small bond length alternation (BLA = 0.05 Å) and bond angle alternation (BAA = 25.3°) within C_{14}. The double bonds indicated by blue and black in C_{14} represent two different bond lengths within the structure, respectively.

C–C	Bond length(Å)	Bond order
1-2	1.2229	2.4457
2-3	1.3456	1.2767
3-4	1.2228	2.4445
4-5	1.3457	1.2760
5-6	1.2229	2.4430
6-7	1.3454	1.2750
7-8	1.2228	2.4390
8-9	1.3457	1.2765
9-10	1.2228	2.4401
10-11	1.3458	1.2786
11-12	1.2229	2.4456
12-13	1.3457	1.2770
13-14	1.2230	2.4446
14-15	1.3458	1.2761
15-16	1.2229	2.4420
16-17	1.3458	1.2769
17-18	1.2229	2.4428
18-1	1.3456	1.2779

C–C–C	Bond angle (°)
1-2-3	159.224
2-3-4	160.819
3-4-5	159.171
4-5-6	160.850
5-6-7	159.122
6-7-8	160.932
7-8-9	159.072
8-9-10	160.864
9-10-11	159.198
10-11-12	160.732
11-12-13	159.249
12-13-14	160.818
13-14-15	159.166
14-15-16	160.855
15-16-17	159.143
16-17-18	160.813
17-18-1	159.222
18-1-2	160.748

Extended Data Fig. 8 | The bond lengths, Mayer bond orders and bond angles in a cyclo[18]carbon. Calculations were conducted at the ωB97XD/6-311 + + G(d,p) level, revealing a bond length alternation (BLA = 0.12 Å) within C_{18}.
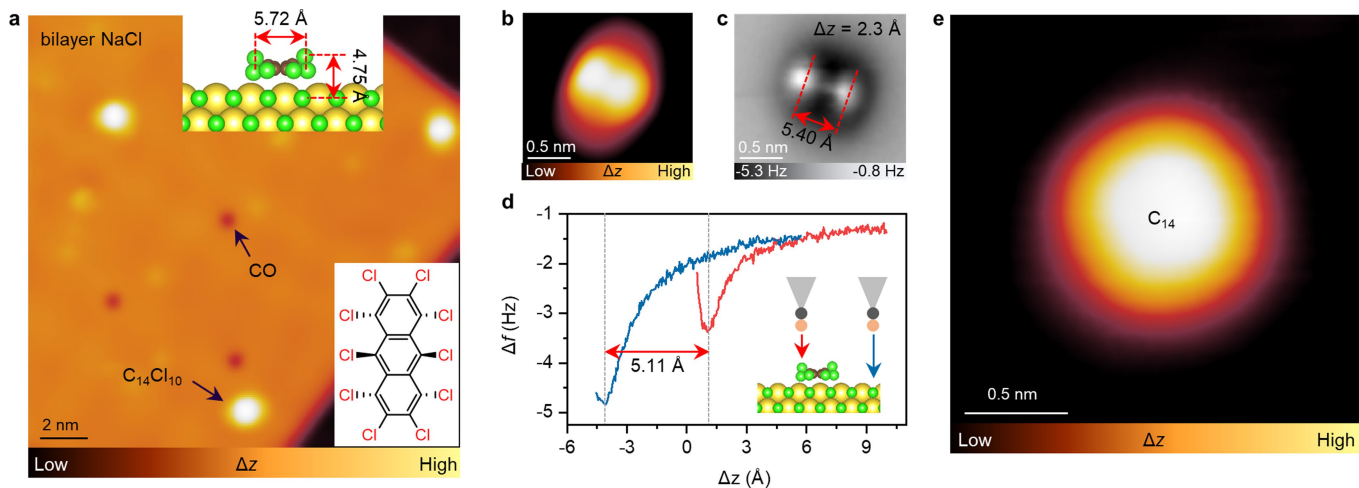
Extended Data Fig. 9 | STM images of the $C_{14}Cl_{10}$ precursor and the product cyclo[14]carbon. (**a**) $C_{14}Cl_{10}$ and CO molecules separately adsorbed on a bilayer NaCl/Au(111) surface. (**b**, **c**) STM and AFM images of an individual $C_{14}Cl_{10}$ molecule. (**d**) Spectra of frequency shift (Δf) as a function of tip height (Δz). The red and blue spectra were taken at the topmost Cl atom of the $C_{14}Cl_{10}$ molecule, and the Cl atom at the first layer of NaCl surface, respectively. Inset: schematics of the CO-tip approaching processes. The distance between two topmost Cl atoms of $C_{14}Cl_{10}$ molecule extracted from the AFM image and experimental absolute height extracted from the spectra reasonably agree with the theoretical values. (**e**) Close-up STM image of C_{14}. Scanning condition: $I = 1$ pA, $V = 0.3$ V for (**a**); $I = 0.5$ pA, $V = 0.3$ V for (**b**); $I = 1$ pA, $V = 0.3$ V for (**e**). Reference set point of Δz for (**c**): $I = 0.5$ pA, $V = 0.3$ V.
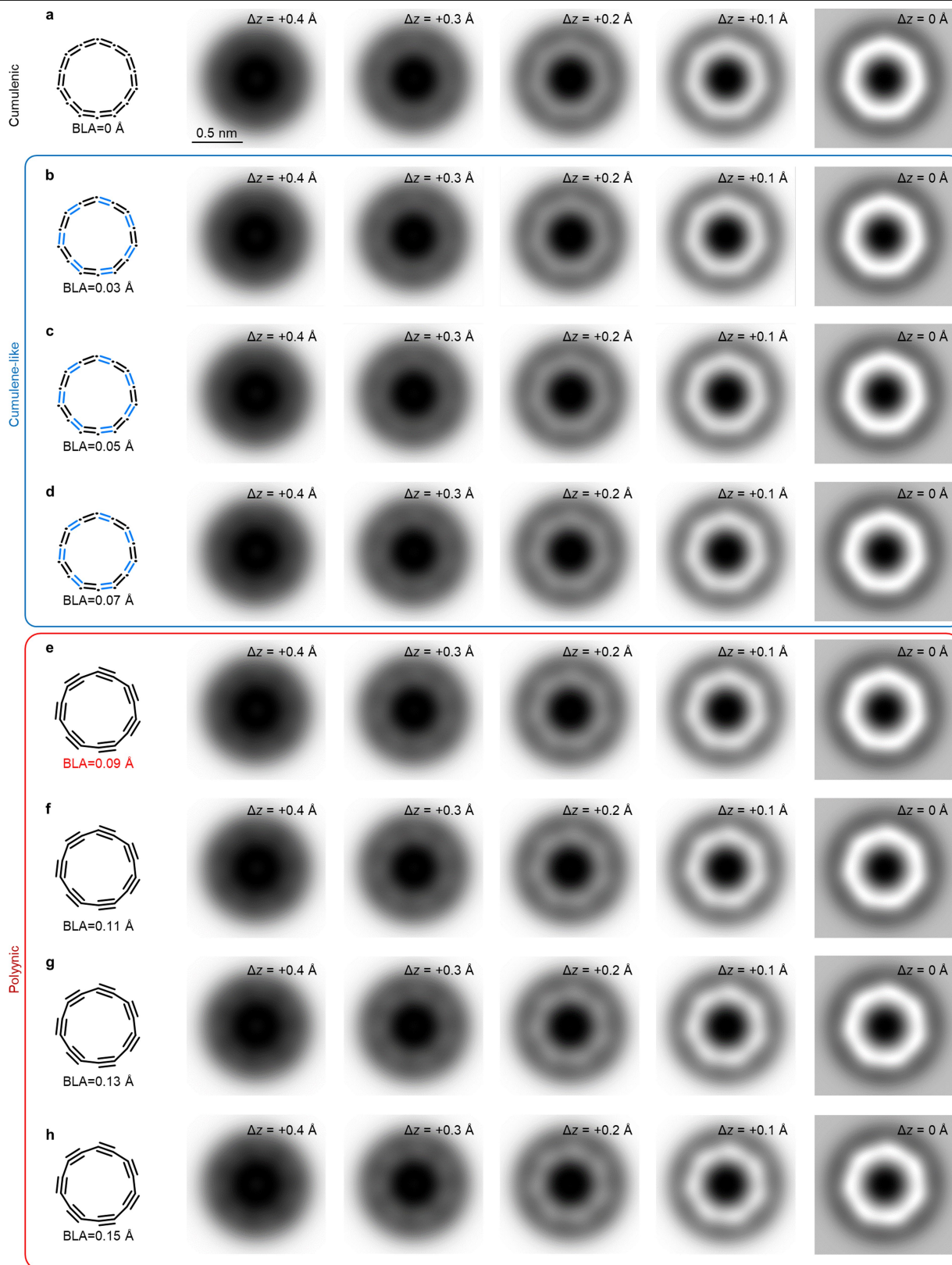
Extended Data Fig. 10 | AFM simulations of C_{14} with varying BLAs.
(**a-h**) A series of AFM simulations of C_{14} with varying BLAs from cumulenic to intermediate to polyynic structures at decreasing tip-sample distances from left to right (i.e., BLA = 0 Å, 0.03 Å, 0.05 Å, 0.07 Å, 0.09 Å, 0.11 Å, 0.13 Å, 0.15 Å) followed by the method developed in ref. 13. The simulated AFM images within blue and red boxes are assigned to cumulene-like and polyynic structures, respectively. All atomic coordinates keep the BAA as 25.3°. The double bonds indicated by blue and black in (**b**), (**c**) and (**d**) represent two different bond lengths within the structures, respectively. The scale bar in (**a**) applies to all simulated AFM images.
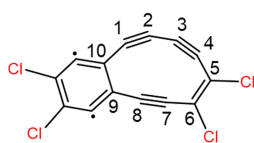
$C_{14}Cl_4$

C-C	Bond length(Å)
1-2	1.2147
2-3	1.3539
3-4	1.2157
4-5	1.3967
5-6	1.3731
6-7	1.4035
7-8	1.2122
8-9	1.4130
9-10	1.4430
10-1	1.4074
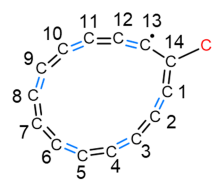
$C_{14}Cl_1$

C-C	Bond length(Å)
1-2	1.2403
2-3	1.3158
3-4	1.2534
4-5	1.3034
5-6	1.2698
6-7	1.2879
7-8	1.2891
8-9	1.2688
9-10	1.3046
10-11	1.2526
11-12	1.3167
12-13	1.2397
13-14	1.3677
14-1	1.3671

Extended Data Fig. 11 | The bond lengths in the $C_{14}Cl_4$ and $C_{14}Cl_1$ intermediates. The bond lengths of a ten-membered carbon ring in the $C_{14}Cl_4$ intermediate (**a**) and a fourteen-membered carbon ring in the $C_{14}Cl_1$ intermediate (**b**) are listed.

Calculations were conducted at the ωB97XD/6-311 + + G(d,p) level. The double bonds indicated by blue and black in $C_{14}Cl_1$ represent two different bond lengths within the structure, respectively.

molecule	AFM	Lap.
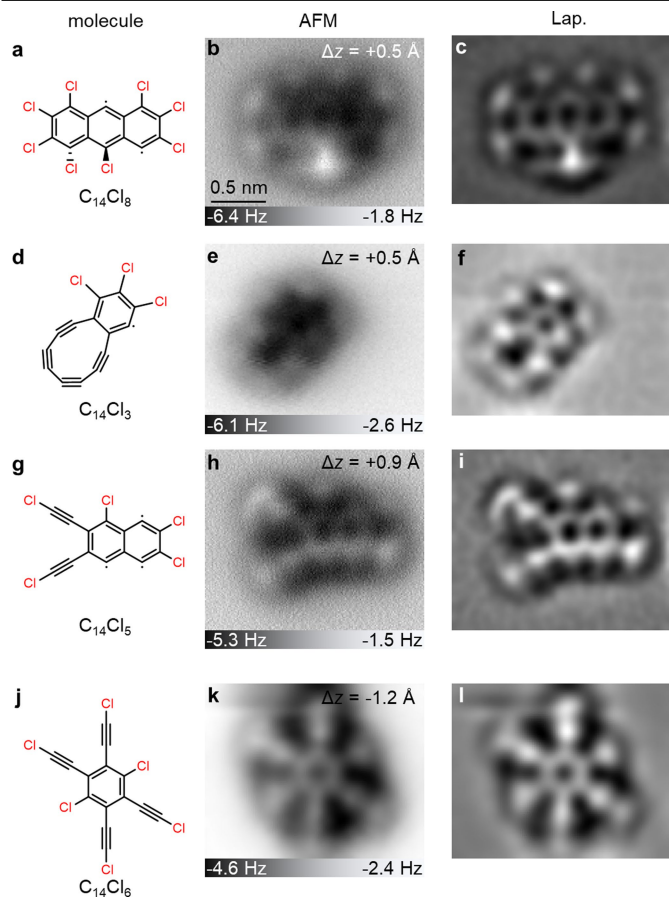
Extended Data Fig. 12 | Other intermediates and side reaction products observed during manipulations. (**a-c**) $C_{14}Cl_8$, (**d-f**) $C_{14}Cl_3$, (**g-i**) $C_{14}Cl_5$, (**j-l**) $C_{14}Cl_6$. The Laplace-filtered AFM images are also shown. Reference set point of Δz: $I = 0.5$ pA, $V = 0.3$ V for (**b**) and (**e**), $I = 1$ pA, $V = 0.3$ V for (**h**), $I = 0.2$ pA, $V = 0.3$ V for (**k**). The scale bar in (**b**) applies to all experimental and Laplace-filtered AFM images.